Linköping Studies in Science and Technology
Licentiate Thesis No. 1442

Nanostructuring and Age Hardening in TiSCN, ZrAlN, and TiAlN Thin Films

Lars J. S. Johnson

Linköping University
INSTITUTE OF TECHNOLOGY

LIU-TEK-LIC-2010:13
Thin Film Physics Division
Department of Physics, Chemistry, and Biology (IFM)
Linköping University
SE-581 83 Linköping
Sweden

ISBN: 978-91-7393-370-4
ISSN: 0280-7971

Printed by LiU-Tryck

To Alchemists

If all you boast of your great art be true;
Sure, willing poverty lives most in you.

—Ben Jonson

Abstract

This thesis explores nanostructuring in TiSiCN, ZrAlN, and TiAlN thin films deposited by cathodic arc evaporation onto cemented carbide substrates, with intended applications for cutting tools. The three systems were found to exhibit age hardening upon annealing, by different mechanisms, into the superhard regime (≥ 30 GPa), as determined by a combination of electron microscopy, X-ray diffraction, atom probe tomography, ERDA, and nanoindentation techniques. TiSiCN forms nanocomposite films during growth by virtue of Si segregation to the surface of TiCN nanocrystallites while simultaneously promoting renucleation. Thus, the common columnar microstructure of TiCN and low-Si-content (≤ 5 at. %) TiSiN-films is replaced by a "feather-like" nanostructure in high-Si-content (≥ 10 at. %) TiSiCN films. The presence of C promotes the formation of this structure, and results in an accelerated age hardening beginning at temperatures as low as 700 °C. The thermal stability of the TiSiCN films is, however, decreased compared to the TiSiN system by the loss of Si and interdiffusion of substrate species; C was found to exacerbate these processes, which became active at 900 °C. The ZrAlN system forms a two-phase nanostructure during growth consisting of cubic ZrAlN and wurtzite ZrAlN. Upon annealing to 1100 °C, the c-Zr(Al)N portion of the films recovers and semicoherent brick-like w-(Zr)AlN structures are formed. Age hardening by 36 % was obtained before overageing sets in at 1200 °C. As-deposited and annealed solid solution $Ti_{0.33}Al_{0.67}N$ thin films were characterized for the first time by atom probe tomography. The as-deposited film was found to be at the very initial stage of spinodal decomposition, which continued during annealing of the film at 900 °C for 2 h. N preferentially segregates to Al-rich domains in the annealed sample, causing a compositional variation between Ti-rich and Al-rich domains, to maintain the stoichiometry for the developing AlN phase. That effect also compensates for some of the coherency strain formed between cubic domains of TiN and AlN. Finally, a possible Kirkendall effect caused by an imbalance in the metal interdiffusion during the spinodal decomposition was discovered.

Preface

This thesis is a part of my doctoral studies in materials science, and the field of thin film physics. It is the result of three years' work, in the second theme of FunMat, a VINN Excellence centre, which is tasked with developing deeper understanding and new technologies, in collaboration with the Swedish cutting tool industry. This thesis is my first, small, contribution to this aim.

—Lars Johnson

Acknowledgments

I am indebted to many people for helping me during the course of this work, so I would like to give my heartfelt thanks to:

Lars Hultman, my main supervisor, for opening my eyes to materials science and electron microscopy, and for your inexhaustible supplies of ideas and energy.

Magnus Odén, my other supervisor, for helping me out, with encouragement and sensible ideas.

Krystyna Stiller, for initiating me into the esoteric world of the atom probe.

Lina Rogstöm, Mats Johansson and the rest of Theme 2 of FunMat, for your support and friendship.

Lars-Alfred Engström and Peter Münger, for teaching me how to teach.

The Thin Film, Nanostructured Materials, and Plasma groups, as well as all other friends at the department, for being great friends; whether for lunch, coffee, or partying.

The Microscopy and Microanalysis group at Chalmers Technical University, for making me feel at home away from home.

My family.

Included Papers

Paper I

Microstructure Evolution and Age Hardening in (Ti,Si)(C,N) Thin Films Deposited by Cathodic Arc Evaporation
L. J. S. Johnson, L. Rogström, M. P. Johansson, M. Odén, L. Hultman
Submitted for publication

Paper II

Age Hardening in Arc-evaporated ZrAlN Thin Films
L. Rogström, L. J. S. Johnson, M. P. Johansson, M. Ahlgren, L. Hultman, M. Odén
Scripta Materialia 62 (2010) 739–741

Paper III

Spinodal Decomposition of $Ti_{0.33}Al_{0.67}N$ *Thin Films Studied by Atom Probe Tomography*
L. J. S. Johnson, M. Thuvander, K. Stiller, M. Odén, L. Hultman
In manuscript

Contents

1 Introduction

Hard coatings, or more specifically, hard ceramic thin films, have been used on tools for metal cutting since the 1970s [1]. Today, more than 80 % of produced cutting inserts for metal cutting are coated [2]; this results in an increase in lifetime (or productivity) of several hundred per cent compared to uncoated tools [3]. The first coatings were TiN or TiC, but the industry has since moved to more complex material systems, such as TiCN, TiAlN, TiSiN or Al_2O_3, and there is a constant drive towards better performing coatings.

Parallel to this development in industry, progress has taken place in the research field of thin films. TiN is the archetypical hard coating, and has been studied extensively [4–6], both as a model system to understand deposition techniques, and for its properties when deposited as a thin film. Often research has followed industrial applications, trying to answer the question of why a particular material performs well. Examples are TiCN [7], TiAlN [8] and TiSiN [9]. These investigations ultimately lead to better understanding of the relationship of structure and properties, which may then be used to develop better-performing thin films.

TiAlN is a good example in this regard. Originally, Al was added to TiN with the intention to improve the high temperature oxidation resistance of TiN. The machining performance of cutting tools coated with the new material was indeed improved [10 and 11]. It was realized that the Ti-Al-N thin system contained a miscibility gap; Al is not soluble in NaCl-TiN [12]. This leads to a decomposition of solid solution films deposited far from equilibirum upon annealing. When studying this decomposition Hörling *et al.* discovered that these films also age harden [13]. This effect has its origin in the changes in the film on the nanoscale, a *nanostructuring*, during the decomposition process. The nature of this decomposition is the subject of one of the papers included in this thesis.

Thus, for modern thin film processing a key element is to understand and control not just the phase and microstructure, but the nanostructure of the film. The nanostructuring of a film may occur either during synthesis, the most extreme case being the deposition of multilayers [14], or during post deposition treatment, but it fundamentally depends on the thermodynamical properties

of the elements involved. Thus, the study of these different processes, whether by growth or post-deposition annealing, may give fundamental insights into the behaviour of this kind of materials.

Thus, the aim of this thesis is the study of nanostructuring in ceramic hard coatings, all with applications in metal cutting, and the effects of such structures on the properties of the films.

Materials

2

Transition metal nitrides (especially those of group IV elements, Ti, Zr and Hf) have several properties that make them technologically important. The first one is their high hardnesses: single crystal TiN has a hardness of 20 GPa [15]. The second is their high melting points [6], around 3000 °C, and they are quite stable against reactions. For example, TiN oxidizes at around 500-600 °C. Due to its wide availability TiN is the most important material of these for structural applications today, although it is often alloyed to further control its properties.

The group IV nitrides share a common crystal structure in the B1 NaCl structure. This is simply two fcc lattices offset by one-half of the lattice parameter, where the metal element atoms occupy one lattice and the nitrogen atoms the other. Another way of visualizing the lattice is to surround each metal atom with eight nitrogen atoms arranged in a regular octahedron.

2.1 Solid Solution Films of Immiscible Nitride Alloys

During experimentation to produce film materials with even better properties than the base binary nitrides, it was discovered that there exist a number of other nitride materials with low or essentially no solubility in TiN. AlN, and SiN_x [10 and 12] are the most well-known and used materials in this class today.

By using certain deposition methods, such as cathodic arc evaporation, it is possible to synthesize homogeneous films with compositions in the miscibility gap, that is, films in a non-equilibrium state.

2.1.1 *Ti-Al-N*

Ti-Al-N was the first metastable alloy to be used by industry as a coating for cutting tools. Aluminium was first added with the intention to improve the oxidation resistance of TiN, as cutting tools may reach over 1000 °C during operation [7]. It is possible to retain the B1 TiN phase with (atomic) a Al content up to of 70 % of the total metal content [12].

Hörling *et al.* [13] were the first to connect age hardening in metastable TiAlN thin films to decomposition into TiN and AlN. Hörling found that the TiAlN film would first decompose into TiN and B1 AlN, and only upon further annealing would the cubic AlN transform into the thermodynamically stable wurtzite phase. The nature of this first decomposition has been the subject of much interest. Calculations [16] suggest that the pseudobinary system $Ti_{1-x}Al_xN$ has a spinodal that covers almost the entire range from TiN to AlN at experimentally accessible temperatures.

2.1.2 *Zr-Al-N*

ZrN is similar to TiN; the crystal structure is the same B1 structure, but ZrN has a larger lattice parameter (a = 4.58 Å [17]) than TiN (a = 4.24 Å [18]). This makes the mismatch between ZrN and AlN bigger as well, as AlN will assume a lattice parameter of ~4.05 Å [19] if forced into the B1 structure. Just as AlN is immiscible in TiN, it is immiscible in ZrN, and experiments indicate that the driving force for segregation is larger in the case of Zr-Al-N. Wong *et al.* tried to stabilize B1-AlN in multilayer stacks of TiN/AlN or ZrN/AlN [20], and while it was possible to stabilize AlN with TiN, it was not possible to do so with ZrN; the result was either amorphous or hexagonal AlN.

2.1.3 *Ti-Si-C-N*

The alloy Ti-Si-N has gathered a lot of attention as it was reported that TiN crystallites (≤ 10 nm in diameter) surrounded by one to a few monolyers of SiN_x, usually referred to as the nc-TiN/a-SiN_x nanocomposite, exhibited an extraordinary hardness of around 50 GPa [21 and 22]. The Ti-Si-N nanocomposite was first synthesized by CVD (see next chapter), but films deposited by magnetron sputtering will typically also have this microstructure. When TiSiN is synthesized by arc evaporation it is possible to produce solid solution films with Si contents up to approximately 5 at. % [9].

Solid solution TiSiN films undergo decomposition when heat treated [9], by segregation and transformation into TiN and SiN_x. The segregation of Si is different from the TiAlN case, as the microstructure of TiSiN films is typically different. Due to the limited solubility of Si in TiN, the films will generally be nanostructured, often with columnar grains around 20-40 nm in diameter. The segregation of Si in this case was shown by Flink to proceed to the grain boundaries, and then, upon further annealing, Si was found to leave the film entirely [9].

A common method of enhancing the properties of TiN for cutting tools is the addition of C, which substitutionally replaces N. TiCN films are stable and do not decompose upon annealing [7]. Ti-Si-C-N deposited by CVD is very similar in properties and structure to nc-TiN/a-SiN [23 and 24].

Phase Decomposition

3

This chapter gives an overview of the mechanisms of phase decomposition. The decomposition processes are important as they are a means to control the structure of a thin film after (or during) deposition by heat treatments. They also affect the stability and performance of coated cutting tools, as cutting operations typically produce high temperatures and pressures. Phase transformations in general is a very extensive topic, so the discussion here is limited to diffusional transformations. For a comprehensive treatment, see, for example, Porter, Easterling and Sherif's *Phase Transformations in Metals and Alloys* [25].

3.1 Phase Stability

A basic result of thermodynamics is that a system is in equilibrium when its Gibbs' free energy is at minimum (or some other thermodynamic free energy, like Helmholtz's free energy; depending on the constraints under consideration). The molar free energy of a phase will vary with composition due to variations in entropy and electronic binding energy; the problem of finding the stable configuration for a composition is thus reduced to the comparison of these curves. There are two possible cases for stability when considering binary alloys, and they are shown in fig. 1. For a given composition, a single phase may have the lowest energy, marked X in fig. 1, or a linear combination of two phases may be lowest, marked Y.

If we have a system composed of one phase at point Y in fig. 1 (such a system may, for example, be obtained by quenching a heated alloy, or by thin film deposition), the system is not at its lowest energy state, and consequently not at equilibrium. For decomposition to take place, atoms need to diffuse, as the equilibrium is a two-phase mixture of different compositions (X and Y'). This is the fundamental limitation of phase decomposition; even if there are no other barriers to the separation, segregation will not occur if the temperature is too low for any appreciable diffusion. This is often referred to as a *kinetic limitation*, as, fundamentally, it is the rate of the transformation that is the limitation.

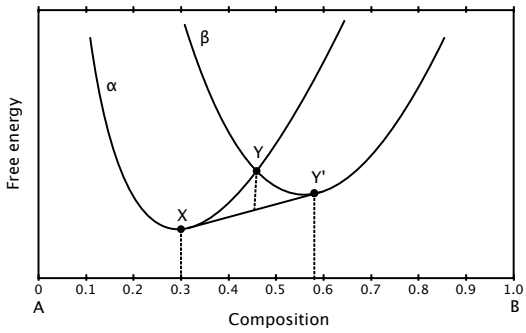

FIGURE 1 Free energy diagram for two hypothetical phases, α and β, of an A-B alloy.

A system in a non-equilibrium state may still be stable against fluctuations, even when diffusion processes are active. This is known as *metastability*. Gibbs considered [26] the kinds of fluctuations a system must be stable against, and arrived at two types: (1) composition fluctuations with small amplitudes and long wavelengths, (2) fluctuations with large amplitudes but small in extent. The first case occurs in spinodal decomposition; the second in classic nucleation.

3.2 Nucleation and Growth

If a system of phase β at composition X in fig. 1 could reconfigure itself into the stable phase α, the free energy would be lowered. This happens during nucleation, when small nuclei of the precipitating phase are formed by thermodynamic fluctuations. Initially, the nuclei will be so small that their surface energy will be larger than the gain from lower binding energy, and therefore unstable. At some point the gain in binding energy will offset the surface energy, and any increase of size beyond this point will therefore be stable.

Once nucleation has taken place, the precipitates will grow by diffusional transport from the matrix phase. The growth might, however, be inhibited in the case of semicoherent interfaces, as the movement of them might require energetically unfavourable transformations of the crystal lattice.

3.3 Spinodal Decomposition

Certain systems are immiscible, i.e. it is unfavourable for their components to mix. A schematic free energy curve for such a system is shown in fig. 2. The

main characteristic of these curves is the local maximum, marked M in the figure. As the local curvature is negative (by definition of a local maximum), any small variation away from a random mixture in this region will lower the total free energy; the system is unstable.

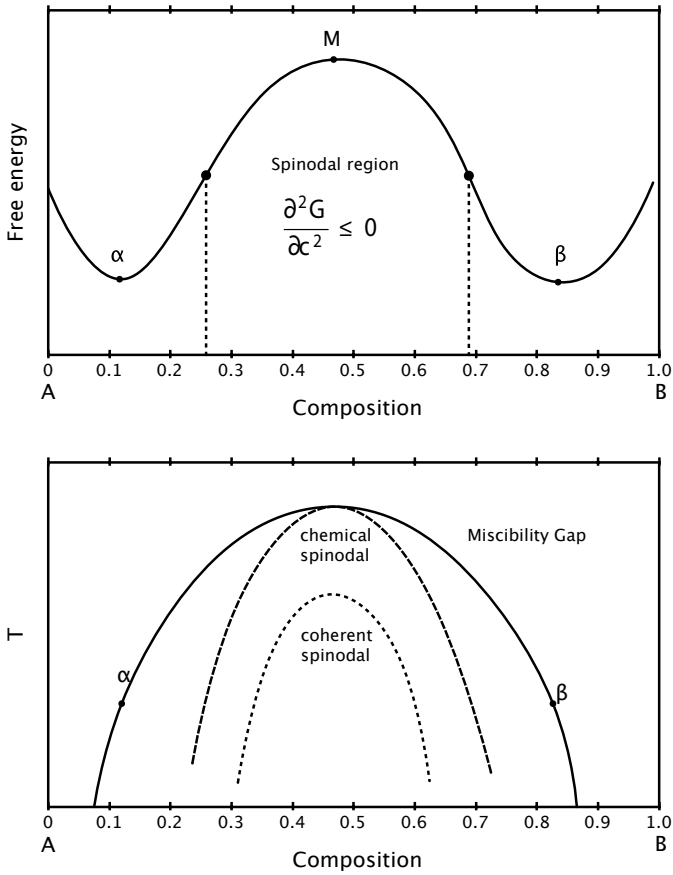

Figure 2 Free energy curve of a system with the potential for spinodal decomposition, and corresponding phase diagram.

The free energy of a system may be written as [27]:

$$F = \int f(c) + \frac{K}{2}(\nabla c)^2 dV, \tag{1}$$

where f(c) is the free energy per unit volume, and the gradient term is the energy associated with forming a gradient in the composition. As we are concerned

with small fluctuations we can Taylor-expand the free energy around the mean composition:

$$f(c) = f(c_0) + \frac{\partial f}{\partial c}|_{c=c_0}(c - c_0) + \frac{1}{2}\frac{\partial^2 f}{\partial c^2}(c - c_0)^2 + \dots \tag{2}$$

To the first approximation the difference in free energy due to the fluctuations will be:

$$\Delta F = \int \frac{1}{2}\frac{\partial^2 f}{\partial c^2}(C - c_0)^2|_{c=c_0}(c - c_0) + \frac{K}{2}(\nabla c)^2 dV. \tag{3}$$

By assuming that the variations in composition have a sinusoidal form: $(c - c_0) = A\cos(kx)$, the integral may be evaluated over the volume V:

$$\Delta F = \frac{VA^2}{4}(\frac{\partial^2 f}{\partial c^2} + Kk^2). \tag{4}$$

The criterion for instability is $\Delta F \leq 0$, which requires that:

$$\frac{\partial^2 f}{\partial c^2} \leq Kk_c^2, \tag{5}$$

where k_c is the critical wave vector for the fluctuations. This means that there is a cutoff wavelength below which fluctuations cannot grow, which is defined by the criterion $\frac{\partial^2 f}{\partial c^2} \leq 0$ that defines the *chemical spinodal*.

The derivation above left out an important part, namely coherency strains. For sinusoidal fluctuations, Cahn [27] showed that the strain energy contribution is:

$$\Delta F_{strain} = \frac{VA^2}{4}\frac{2\eta^2 E}{1 - \nu}, \tag{6}$$

where η is the fractional change in lattice parameter per change in composition, E is the elastic modulus and ν is Poisson's ratio. This in turn, directly leads to a modified stability criterion:

$$\frac{\partial^2 f}{\partial c^2} \leq Kk_c^2 + \frac{2\eta^2 E}{1 - \upsilon}. \tag{7}$$

This limits the region of instability to

$$\frac{\partial^2 f}{\partial c^2} \leq \frac{2\eta^2 E}{1-\upsilon}, \tag{8}$$

which is termed the *coherent spinodal*.

3.3.1 *The Cahn-Hillard Model*

Cahn, building on work by Hillard, derived a continuum model to study the dynamics of spinodal decomposition. This is now known as the Cahn-Hillard equation, and the following are the main results stemming from it [27]:

$$\frac{\partial c}{\partial t} = M\left(\frac{\partial^2 f}{\partial c^2} + \frac{2\eta^2 E}{1-\upsilon}\right)\nabla^2 c - MK\nabla^4 c. \tag{9}$$

This is an approximative equation, as higher order terms in $f(c)$ and ∇c have been ignored. Nevertheless, it gives valuable insight into the decomposition process.

Solutions to the equation have the form:

$$c - c_0 = A(\bar{k}, t)\cos(\bar{k} \cdot \bar{r}), \tag{10}$$

and $A(\bar{k}, t)$ has the form:

$$A(\bar{k}, t) = A(\bar{k}, 0)e^{R(\bar{k})t} \tag{11}$$

$$R(\bar{k}) = -Mk^2\left(\frac{\partial^2 f}{\partial c^2} + \frac{2\eta^2 E}{1-\upsilon} + Kk^2\right). \tag{12}$$

From 7 we see that R will be positive for wave vectors k larger than the cutoff; these waves will grow exponentially in this approximation, with a maximum rate at $k = \frac{k_c}{\sqrt{2}}$. The exponential increase cannot continue indefinitely, and this is recovered if more terms are added to the governing equation [28].

3.4 Age Hardening

Systems that undergo phase decomposition during annealing may also show a consequent increase in their hardness. This is termed *age hardening*, and is a direct result of the changes in nanostructure due to the decomposition. Hardness is, by definition, the degree to which a material is able to resist plastic deformation, i.e. resistance to the generation and movement of dislocations and other defects. In particular, the movement of dislocations is hindered by

the creation of precipitates or composition fluctuations in the matrix, as this will generally introduce strain. Dislocations may either cut through or bow around precipitates, and both are usually more difficult than passage through a homogeneous lattice. If the annealing is continued for too long the system will transform into its equilibrium phases and any hardening effects will be lost.

A convincing example of age hardening in thin films is found in solid solution TiAlN [13]. As mentioned in the previous chapter, c-TiAlN will decompose upon annealing, first to TiN and c-AlN parts (800-900 °C), followed by a transformation into h-AlN at higher temperatures (~1100 °C). The age hardening is in effect during the segregation into cubic phases, but is generally lost upon formation of the hexagonal AlN phase.

Deposition

4

The act of creating a thin film is called *deposition*, recalling both the creation of the whole film and the placement of individual atoms in it. There are many different ways of depositing a thin film; the most common ones are based on deposition from a vapour of some sort (as opposed to wet chemical methods, for example). These techniques may further be subdivided into *Physical* Vapour Deposition (PVD) and *Chemical* Vapour Deposition (CVD). The difference is in the vapour: in PVD the vapour is composed of atoms and molecules that simply condense on the substrate, whereas in CVD the vapour undergoes a chemical reaction on the substrate, the product of which forms the film. This work is solely focussed on PVD methods.

4.1 Physical Vapour Deposition

The perhaps simplest PVD method is thermal evaporation, in which the source material is evaporated (or sublimated) in one end of an evacuated chamber and deposited on the substrate at the other, colder, end of the chamber. This captures the basic process of PVD; first a vapour is produced, then it is transported to a substrate and made to deposit there. What separates the different techniques is the method of vapour production, its dependent properties, and the level of control available over the deposition.

4.1.1 *Cathodic Arc Evaporation*

Cathodic arc evaporation is a technique that is widely utilized in the coating industry, especially in the cutting-tool industry, as it is a superior method of producing hard adherent coatings. The technique also has drawbacks, in that the films tend to be in a compressive stress state, which limits coating thickness and the so-called macro-particles produced by the evaporation that are embedded in the film.

As the name implies, the source material is evaporated by an intense cathodic arc, produced by negatively biasing the target and triggering a dielectric breakthrough by striking the target – or *cathode* – with a sharp pin. The spot

on the cathode where the arc hits is locally melted, and atoms are ejected away from the surface in an almost completely ionized state (typically greater than 95 %) and with high kinetic energies (20-200 eV dependent on material [29]. Along with the ionized flux, macro-particles are also ejected; these are particles of molten and semi-molten target material that are produced by the pressure of the arc spot on the molten zone in the cathode. Arc evaporation may also be run reactively, to deposit a nitride thin film, for example; then it is common to combine the arc evaporation with a glow discharge to help crack the gas molecules.

Due to the high currents needed to sustain the arcing, the cathode material must be conductive. A further practical limitation is given by the melting point of the cathode material; the higher the melting point the harder it will be to arc evaporate.

Thin films produced by cathodic arc evaporation are typically dense, in a compressive stress state and very defect rich. This is due to the high kinetic energies of the incident ions, which produce collision cascades in the growing film that tend to create point defects. The adhesion of arc evaporated films is often better than of comparable films from other PVD methods, and this is again due to the energetic ions, which produce a mixed interface by implantation in the substrate. By applying a high bias to the substrate, the effect of implantation may be enhanced, either for implantation treatments or for etching of the substrate at higher voltages.

4.2 Film Growth

The two deciding factors of how a film grows are the substrate temperature and the flux and energy distribution of the incident species. These parameters determine the *kinetics* of the growth. As a rule of thumb, the more energy that is available during growth, the closer the structure will be to thermal equilibrium. The two properties of the growing film that are of interest are its *phase* and *microstructure*.

4.2.1 *Phase*

The phase of a thin film – even for a constant composition – may vary widely with deposition conditions. In the case of kinetically limited depositions, it is not uncommon for the films to be amorphous, as the incident atoms just quench directly on their site of arrival with minimal diffusion. Provided with more energy, the arriving atoms will diffuse and form crystalline clusters. The

nature of the phases that form is determined by the thermodynamically stable phases at the growth conditions, but is also influenced by the surface energies of the substrate and vacuum interfaces. The stability may also be affected by the bombardment of incident species, given high enough energies per atom.

4.2.2 *Microstructure*

The microstructure of a film depends on the processing parameters. At low surface diffusivities adatoms will nucleate at many points on the substrate, and these nucleation sites will grow into individual columnar grains. At higher diffusivities the adatoms will be able to travel greater distances, which gives fewer and bigger grains. At even higher temperatures the film may recrystallize during growth, transforming the growing columns to an equiaxed grain structure. These possibilities are often summarized in a structure zone model (SZM) diagram [30], and one suitable for PVD is given in fig. 1. Films deposited by arc evaporation typically fall into the mid zone of this diagram, with a dense columnar microstructure. Columns frequently grow in competition with each other, where the growth rate often depends on the crystallographic orientation of the column [31].

The orientation of the grains may vary or be templated from the substrate, but it is often the case, that different orientations of grains will grow with different speeds due to differences in surface diffusivity. If this is the case a film may almost completely consist of columns with a certain orientation even though the grains originally nucleated with a variety of orientations.

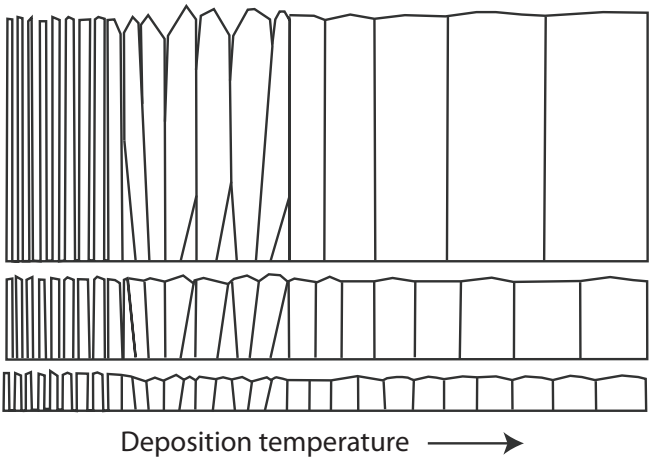

FIGURE 1 Structure zone model for PVD after Barna *et al.* [30]

5 Characterization

To study thin films, and processes in thin films such as age hardening, we must know the state that the film is in. We need to know the phase(s), the composition (both on macro- and microscales), the microstructure, and eventual nanostructure, and so on. This understanding is gleaned from the combination of several characterization techniques, as a single technique seldom gives the whole picture needed. In this chapter, the main characterization techniques used in this thesis are presented.

5.1 X-Ray Diffraction

Due to the periodic ordered structure of a crystal, X-ray waves scattering against the atoms in a crystal will produce interference reflexes in certain directions, which are tied to the crystal structure and the specific orientation of the incident wave. This effect is utilized in the various techniques of X-Ray Diffraction (XRD) to investigate the crystal structure of a sample, as well as structural properties such as grain size, texture and the thickness of a thin film.

The basic principle of XRD is most easily understood as positive interference of waves scattered against adjacent planes in the crystal. This gives rise to Bragg's Law:

$$2d\sin(\theta) = n\lambda. \tag{1}$$

A more useful description is due to von Laue, who described diffraction in reciprocal space with the diffraction condition: $\overline{k_i} - \overline{k_f} = \overline{\Delta k} = \overline{G}$, where $\overline{k_1}$ and $\overline{k_f}$ are the wave vectors of the incident and scattered waves, respectively, and G is a reciprocal lattice vector. This formulation leads directly to the interpretation of the shape of a reflection as that of the shape of the respective reciprocal lattice point, which in turn is due to deviations from the theoretical infinite periodic crystal lattice.

The most basic XRD method is the θ-2θ scan (sometimes referred to as the Bragg-Brentano geometry) in which the incidence and exit angles are varied symmetrically. This limits the difference in wave vectors for the incident

and scattered beams to being parallel to the surface normal of the sample. By assigning the observed peaks in a scan to a crystal structure, the lattice parameter may be measured from the position of the reflections. Care must be taken, however, as the lattice parameter may be significantly shifted by strain in the samples – due to film-substrate strain or strain from atom peening during deposition in thin films, for example. The width of a peak is dependent on the average size of a coherently scattering region – most often taken as the grain size – and any local variations in the lattice due to defects, as well as the limitations posed by the instrument used.

A view of any texture of the sample is given by the relation of the various peak intensities and how they deviate from theoretical values. The view is partial, as only scattering regions with planes parallel to the surface are probed in the method. For a fuller analysis of texture, complementary techniques are required, such as pole figure analysis, where a certain reflection is selected and then mapped by rotating the sample.

To measure the strain in a thin film the $\sin^2(\psi)$ is a commonly used method. The change in peak position is measured as the sample is tilted away from the symmetric θ-2θ geometry, thus probing the change in lattice parameter as a function of angle to the surface normal. Assuming a biaxial stress state, the stress may then be derived from elastic theory. This biaxial stress state is the typical situation for hard coatings, as they are typically strained compressively against their substrates.

5.2 Transmission Electron Microscopy

Transmission electron microscopy (TEM) is one of the most versatile techniques available for analysis of thin film samples. In different configurations, information on the crystal structure, microstructure, local chemical composition, and bindings, as well as interfacial relations and defects, may be gained. The main drawback of the technique is the extensive sample preparation necessary, potentially introducing artifacts, as well as the small volume probed.

The basic principle of a TEM is that a beam of electrons is shone through a thin foil and the scattered electrons are focused by an electromagnetic lens into an image which is collected as intensities on a view screen or ccd-camera. While the actual details of a TEM are far more complex this is still a fair description of the Bright-Field mode of TEM (so named after the light microscopy technique it mimics). Here contrast in the image is formed either through mass-thickness contrast or diffraction contrast phenomena. Mass-thickness contrast is due to

denser or thicker regions scattering or absorbing more of the electron beam, respectively. Diffraction contrast is due to the blocking of diffracted beams, so that they are not projected back onto the image of their origin by the objective lens. This means that grains oriented such that they are in a strong diffracting condition will appear darker than other grains. Diffraction contrast may also appear locally due to strain in the foil, from bending of the sample or the strain field around a dislocation, for example, which allows the imaging of individual dislocations.

The dark-field mode is closely related to the bright-field mode and has again gained its name from light microscopy. By selecting one (or more) diffracted beams and eliminating the transmitted beam, instead of filtering out all diffracted beams as in the BF-mode, an image is formed with crystallographic information from the selected reciprocal lattice point.

5.2.1 *Electron Diffraction*

As alluded to in the section above, electron waves that interact with a crystal undergo diffraction scattering in the same general way as X-rays do. There are differences – electrons interact with the crystal potential from the atomic nuclei while X-rays scatter against the tightly bound core electrons in the crystal – but these are in most cases of lesser importance when analyzing thin films.

As transmission electron microscopy is fundamentally an imaging technique, the common view of diffraction is the diffraction pattern, which is essentially the result of testing all possible scattering vectors perpendicular to the incident beam. A consequence of the control over the incident electron beam afforded by the illumination part of a TEM is that there are two fundamental modes of diffraction in the TEM, called Selected Area Electron Diffraction (SAED) and Convergent Beam Electron Diffraction (CBED). In SAED the illumination is kept as parallel as possible – ideally projecting reciprocal lattice points to points on the diffractogram – and the name stems from the fact that one most often limits the area contributing to the pattern on the sample by an aperture in the image plane of the aperture. CBEDon the other hand uses a convergent beam, with the beam is at its largest convergence angle, and as such, points in reciprocal space are projected as disks, the diameters of which are inversely proportional to the convergence angle. Here, information is gained from a limited part of the sample (unlike when using SAED). For thicker samples, CBED patterns may also contain information from dynamical diffraction effects, which show up as variations in intensity inside the diffraction disks.

Electron diffraction is an easy way to look for any possible texture in thin films, as a fully random ordering will produce rings in the diffraction pattern spaced according to the plane spacings for all orientations of the sample, whereas the pattern of a sample with a texture will – for some orientations – show gaps in the rings.

Compared to to X-ray diffraction the various electron diffraction techniques are less powerful or precise for determining accurate plane spacings or peak shapes, due to the nature of the TEM. To reach the screen, the diffracted beams are magnified by electromagnetic lenses which introduce uncertainty, and even if that is eliminated – for example, by using a standard sample as reference – the recording of the pattern on either film or ccd is not as precise as the dedicated instrumentation of a XRD instrument. Hence, electron diffraction is best used to discern patterns and symmetries. On the other hand; ED has one advantage over XRD, namely the substantially lower wavelength of high energy electrons as compared to X-rays. A typical X-ray radiation used in XRD is from the CuK_α emission line at 1.54 Å, to be compared with the 2.5 pm relativistic de Broglie wavelength of an electron at 200 keV. This allows smaller scattering regions to be imaged without excessive peak broadening that limits XRD analysis of regions smaller than 10-20 nm.

Finally, electron diffraction is used to precisely align samples for other imaging techniques in the TEM specifically for HRTEM.

5.2.2 *High Resolution TEM*

In electron microscopy the term 'high resolution' has a special significance, in that it implies the direct imaging of the crystal lattice. Resolving the lattice planes – or even individual atom columns – allows the microscopist to image structural configurations on the nanoscale, such as grain boundaries, dislocations, nanoscaled grains themselves, interfaces such as substrate-film or multilayer relationships, and of course the crystal structure itself.

The contrast mechanism in HRTEM is *phase contrast*, that is, contrast due to interference of electron waves producing variations in intensity which we observe in the microscope. The electron wave incident on the sample is diffracted against the lattice planes, and these waves will interfere with the unscattered beam and each other (a more correct and complex view is that the electron wave-function interferes with itself). This produces an *exit wave* that the objective lens then transforms to an image which is projected on the viewscreen in the microscope. Due to the electromagnetic nature of the objective lens it is limited in how it transfers information; this is described by the contrast transfer function (CTF) of the lens is which most often used in frequency space:

$$\mathrm{CTF}(u) = E(u)\sin(\chi(u)). \tag{2}$$

Here E(u) is an envelope function that dampens the transfer of high-frequency signals and so limits the available resolution, and $\chi(u)$ depends on the lens aberrations, which are dominated by the spherical aberration for an ordinary EM-lens. The control and effective elimination of this aberration has become possible with the latest generation of microscopes, and as such they are often called aberration corrected microscopes (or C_s-corrected microscopes, as C_s is the name given to the spherical aberration).

5.2.3 *STEM and Analytical TEM*

A radically different way of producing an image in a TEM is the Scanning TEM mode, in which the electron beam is condensed down to as fine a point as possible which is then rastered across the sample. Contrast is then formed by recording the intensity of the scattered beam and assigning that value to the raster position. Most commonly, a High-Angle Annular Dark Field detector (HAADF) is used as the detector, recording the intensity scattered far out in the diffraction image from the sample. This will then detect differences in average atomic scattering factors, whose dependence on Z-value becomes larger for larger scattering angles.

Today STEM is often coupled with spectroscopic methods – the two main ones being Energy Dispersive X-ray Spectroscopy (EDS) and Electron Energy-Loss Spectroscopy (EELS) – to access the local chemical composition of the sample. For each point in the STEM raster, one or several spectra are recorded; these spectra may then be analyzed and images of variations of features (integrated peak height of an X-ray emission line, for example) produced.

5.2.4 *Electron Energy Loss Spectroscopy*

As the name implies, in EELS the signal of interest is the energy loss of the electrons that have been transmitted through the sample. These electrons have a certain probability of interacting with the electrons present in the sample; in these interactions they lose energy that is characteristic of the actual interaction. The two main interactions that are present in an EELS spectrum are interaction with the valence electrons to excite plasmons (called plasmon loss) and interaction with the core electrons, which are then ejected from their shells (core loss).

A typical spectrum plotted as energy loss versus intensity is dominated by the *Zero-loss peak*, as most electrons do not undergo any losses at all when passing through a thin sample. The second largest feature will be the plasmon peak(s), situated in the region of 1000 eV. Core loss peaks are found on the tail of the plasmon peak, at the corresponding binding energy of the core electron ejected in the interaction. A typical spectrum showing these two regions is shown in fig. 1.

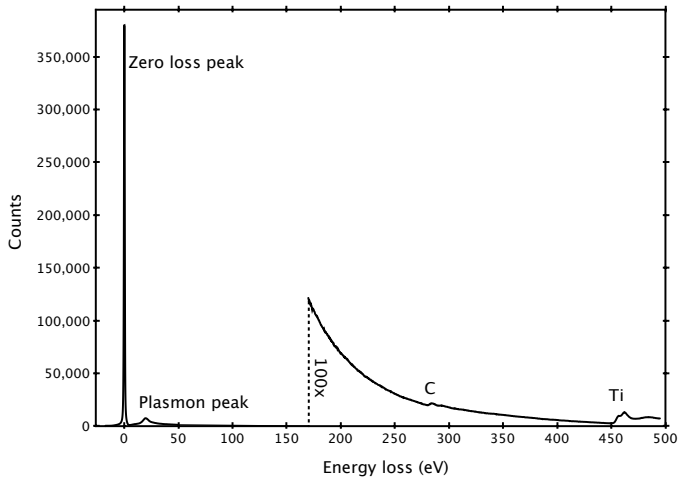

FIGURE 1 A typical EELS-spectrum, showing both the low-loss and core-loss regions

When a core electron is ejected from its shell it must be excited to a vacant quantum state above the Fermi level, and hence the core loss peak (or edge) will have the shape of the electron density of states above the Fermi level multiplied with the transition probability. The core loss peaks are much weaker in intensity than the plasmon peaks due to a smaller cross-section, and because of this, background subtraction is essential to their analysis.

As a sample gets thicker the probability of multiple scattering increases, and this is the fundamental limiting factor of EELS analysis of samples. Each additional scattering will convolute the original signal with the second scattering event, and as plasmon scattering is most likely this will dominate and broaden peaks until they are no longer detectable.

5.2.5 *Energy-Dispersive X-ray Spectroscopy*

The electrons in the beam may interact with atoms in the sample, and while EELSdeals with the measurement of that interaction's effect on the beam, X-ray

spectroscopy may be used to detect the effect on the sample itself. As core electrons are removed from their shells, the atom is no longer in its ground state and will hence relax. This is achieved by the filling of the hole by an electron from a higher shell according to quantum transition principles. The excess energy is then released either as a photon (most often in the X-ray part of the spectrum) or an Auger electron. Due to the limited possibilities for de-excitation, the spectrum of the emitted X-rays acts as a fingerprint for the elements.

Energy-dispersive X-ray spectroscopy is a technique for measuring the emitted X-rays. The term 'energy-dispersive' relates to the detection of the X-rays, and stands in contrast to 'wavelength-dispersive' spectrometers. The term comes from the use of a solid state Si-Li detector in which electron-hole pairs are generated by the incident X-ray photons. The number of pairs are dependent on the energy of the photon, which may then be derived by counting the pairs created.

The counting mechanism is the fundamental limitation of the energy-dispersive spectrometer, as a certain time is needed to count the pairs, and the precision depends on the time spent. To avoid miscounting two photons as one, the counting time must be sufficiently small in relation to the flux of photons to avoid miscounting, and this limits the energy-resolution.

Another issue is the detection of light elements. This is often problematic, as the window between the detector and the microscope's column will tend to absorb the characteristic X-rays of light elements, greatly lowering their detection rate. Notably, this applies to the detection of carbon and nitrogen.

5.3 Atom Probe Tomography

Atom probe characterization has long been a highly esoteric technique; impressive in its power of imaging, but limited in its applicability. This is rapidly changing today, as advances in the instrumentation have allowed the technique to be applied to a much wider range of materials. At its core, a *Field Ion Atom Probe* works by sequentially field-evaporating a sample shaped into a sharp tip, atom by atom. The ions are accelerated towards an area detector at which both the position and the time of flight are measured. A three-dimensional model of the sample is *reconstructed* from this data, essentially by back-projection in both space and time. Thus the atom probe is not a true microscope, and it is not an *imaging* technique, but rather a destructive tomographic technique [32 and 33]. A typical reconstruction of a decomposed sample is shown in fig. 2.

The atom probe evolved from the field ion microscope, which is a true imaging technique. In FIM a sharp tip is placed in an evacuated chamber which is then filled with a analyzing gas, such as helium. The tip is positioned in front of a circular electrode behind which is an fluorescent screen. A voltage is applied between the tip and the counter-electrode, positively biasing the tip, which creates a strong electric field. The field is strongest at the surface of the tip, particularly at the sites of atoms, and by adjusting the applied voltage, gas molecules at the surface are ionized at the sites of atoms. The ions are accelerated by the field, and eventually strike the fluorescent screen, forming a magnified image of the tip.

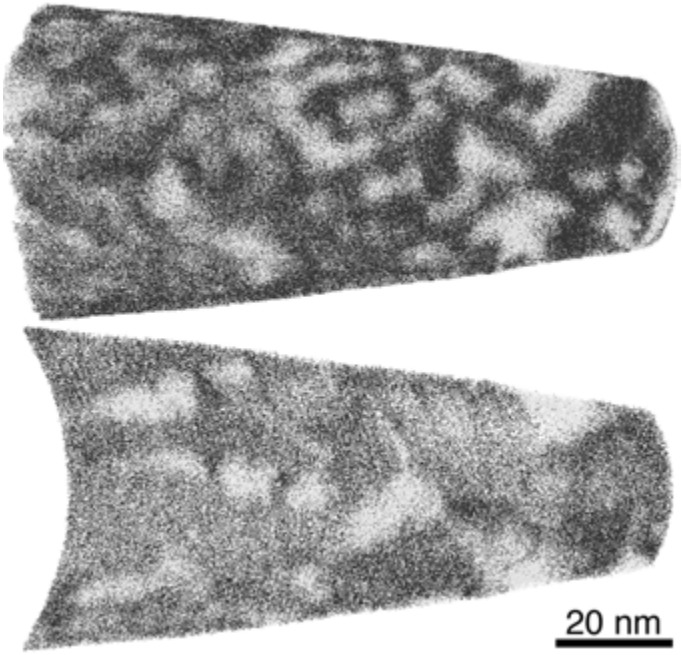

FIGURE 2 Reconstruction of a decomposed TiAlN sample. Only Ti and Al atoms are shown. The second image shows a slice through the centre of the reconstruction.

Increasing the applied voltage further in the FIM eventually causes atoms in the sample to *field evaporate*. The atom probe utilizes this effect by controlling the evaporation – by pulsing the applied voltage, in the simplest case – so that each ion that leaves the sample may be measured for time-of-flight spectroscopy. The fluorescent screen is replaced by a micro-channel plate to record where and when the ion hit. This data is then used in a tomographic reconstruction

of the tip, which is the resulting data of the method, which may be analysed further depending on the specific questions under consideration [34–36].

For a long time the atom probe was limited to conductive samples, as the high stresses of voltage pulsing simply causes tips of insulating samples to shatter, or 'pop' as it is called in the jargon of the field. The first improvement that directly addressed this was the local-electrode atom probe, developed by Thomas Kelly and later commercialized as the LEAP [37] instrument family. Here the counter-electrode is placed just tens of microns from the apex of the sample tip. This makes the electric field much stronger for a given voltage, thus lessening the stresses needed for voltage-induced field evaporation. This allows some more materials, most notably silicon, to be analyzed, but a large class of materials, e.i. brittle ceramics with low conductance, is still impossible to run in the voltage mode today.

The way around this proved to be controlling the specimen temperature by hitting it with a focussed pulsed laser. This causes local heating of the tip, and so gives the atoms in the tip more energy to overcome the barrier for field evaporation. A schematic drawing of a laser atom probe experiment is shown in fig. 3. Even such a refractory material as alumina has been successfully analyzed with the laser-assisted atom probe.

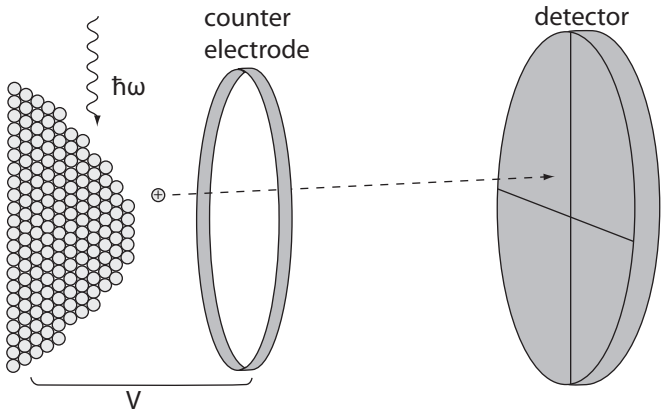

FIGURE 3 Schematic drawing of a laser-assisted atom probe

5.3.1 *Field Evaporation*

While we still do not possess a true quantum mechanical description of field evaporation, there is nevertheless a basic understanding of the process grounded in classical physics. An in-depth review of field evaporation is given by Forbes [38]; what follows here is a summary of the main ideas. If we consider an atom

on a surface, it will have a potential energy function somewhat akin to the Lennard-Jones potential: repulsive close to the surface and zero at infinity, with a minimum at the rest position of the atom. If we consider an ion instead of an uncharged atom, the application of an electric field wil cause the potential energy to slope down to the applied potential far out from the surface; an energy barrier may or may not exist between the local minimum depending on the applied voltage. Now, a 'real' atom will most probably neither be wholly ionized or without charge, as the valence electrons around the atom are not frozen. This leads to a *charge-draining* as the atom moves further from its minimum, which in turn changes its potential energy. At some point an atom will get sufficiently far away and overcome the energy barrier, and has gained an integral ionization: it has now been field-evaporated and is free to accelerate towards the counter-electrode.

The basic physics of this process may be modelled by an Arrhenius equation, with the evaporation frequency, k, given by a Boltzmann factor:

$$k = k_0 e^{-\frac{\Delta E}{kT}}, \tag{3}$$

where k_0 is the test frequency and ΔE is the energy barrier for evaporation. Forbes [38] showed that, at least for small values of the rate, the energy barrier may be written as:

$$\Delta E = B(\frac{F_e}{F} - 1)^2, \tag{4}$$

with B being an empirical constant, F_e being the field where ΔE is zero and F simply the applied field.

Most often the field-evaporated ion will be singly ionized as it overcomes the potential barrier for evaporation, but detected ions are often doubly or triply charged. This discrepancy is explained by the fact that electrons may tunnel from the ion to the surface for a short while after it has left the surface. This is called *post-ionization* and was first described by [39]. This process depends on the applied field and temperature of the sample.

5.3.2 *Reconstruction*

The tomographic reconstruction currently in use for the atom probe (developed by Bas *et al.* [40]) has two fundamental parts: the back-projection of the detector coordinates X_D and Y_D to the sampled coordinates x and y, and the calculation of the depth coordinate z.

The magnification of the atom probe may be modelled as that of a point projection microscope, which gives the magnification, M:

$$M = \frac{L}{\xi R}, \tag{5}$$

where L is the length from the tip to the detector; R is the radius of the tip, and ξ is a constant to compensate for the fact that the ion trajectories are not fully perpendicular to the tip surface. The tip itself is modelled as a truncated cone capped by a part of a sphere so that the gradient across the interface is continuous. This leads to the simple formulas for x and y:

$$\begin{aligned} x &= \frac{X_D}{M} \\ y &= \frac{Y_D}{M}, \end{aligned} \tag{6}$$

which simply project the detector space coordinates to a point on a flat plane situated at the apex of the tip, which is the intersection of a straight line from the detector point to the point on the actual sample tip.

The z-coordinate is handled entirely differently, as it is fundamentally impossible to measure it from the available data. Hence it must be calculated, and this is done by assigning a small increment in depth to each ion:

$$dz = \frac{\Omega}{S_a}, \tag{7}$$

that is, the volume of the ion, Ω, divided by the detected area of the emitting tip, S_a. The emitting area may also be projected to the detector space by the relation:

$$S_a = \frac{S_D}{M^2}. \tag{8}$$

As the detection efficiency (η) of today's instruments is around 30-40 % this must also be taken into account, which gives the formula for dz:

$$dz = \frac{\Omega M^2}{\eta S_D}. \tag{9}$$

The depth, z, for atom k is then given by the sum of all preceding increments:

$$z_k = \sum_{i=1}^{k} dz_i. \tag{10}$$

The formula given above does not take into account the curved nature of the emitter, and for this an additional correction is needed:

$$z = z_k + z', \tag{11}$$

where z' is given by geometric considerations:

$$z' = R(1 - \sqrt{1 - \frac{x^2 + y^2}{R^2}}). \tag{12}$$

All these equations fundamentally depend on the value of the radius of the tip, and that is estimated by the applied voltage V and the evaporation field of the material, F_e, along with a constant k_f due to the concentration of the electric field at the apex of the tip and other geometric factors of the local environment.

$$R = \frac{V}{k_f F_e}. \tag{13}$$

In the algorithm in use today, ξ, k_f and F_e are assumed to be constant for each reconstruction, which is true for evaporation from single-phase materials.

5.3.3 *Sample Preparation*

The preparation of thin film samples for atom probe tomography is done by the Focussed Ion Beam microscope (FIB) [41 and 42]. The basic procedure is to lift out a piece of the sample and mount it on an appropriate tip, followed by annular milling to form the sharp tip needed for field evaporation. The method used in this work is as follows:

First a protective strip of Pt is deposited, with dimensions 20x2.5x0.5 μm. A wedge-shaped piece of material is then milled free by two trenches angled 30° from the surface normal. If the sample is under a large compressive stress, care must be taken, as the stress may break the sample when it is cut loose from the substrate, especially if the sample is still connected to the rest of the film at the edges of the wedge. Once the sample is cut loose on all sides except on one short edge, it is welded to a micromanipulator needle, cut loose and lifted out.

One wedge may be used to make several tips, so for each supporting tip a part of the wedge is welded to it with Pt and the rest of the wedge cut loose.

The wedge should be aligned so that the laser will hit a side without Pt welds, as the laser may induce Pt migration to the apex of a running tip and there interfere with the experiment. Both available sides on the wedge should be welded, to ensure the strongest weld possible.

Once the wedge is welded in place, annular milling is applied to form the actual tip. Typically a beam of 500-200 pA of 30 keV ions is utilized, with inner diameters starting at 1-1.5 μm and stopping at 200-300 nm for the milling pattern. At this stage the tip must be formed symmetrically, and the Pt layer minimized, but not fully removed. Care should also be taken to minimize the damage to the post to avoid breaking during analysis. The final step is to remove the remaining Pt layer and sharpen the tip. This is achieved by milling the entire apex region with 5 kV ions until a good shape is formed.

5.4 Elastic Recoil Detection Analysis

Erda is a technique for compositional analysis, in which high energy ions (typically in the MeV range) of a heavy element are directed at an angle onto the sample of interest. Elements lighter than the incident ions will then be emitted from the sample due to elastic collisions. By detection of both ion mass and energy, compositional depth profiles may be constructed from the data. The technique is able to detect all elements that are lighter than the incident ion at depths approaching 1 μm.

5.5 Nanoindentation

Nanoindentation is a technique to determine mechanical properties (primarily hardness) of a sample. A sharp, hard tip (most often of diamond) is pushed into the sample as the depth and load required are recorded. This forms an *indentation curve* from which it is possible to extract, for example, the hardness by fitting parts of the curve to a model.

The most widely used model is due to Oliver & Pharr [43], where, by contact mechanics, the elastic modulus is determined as a function of the slope of the start of the unloading curve, the elastic modulus of the diamond indenter and Poisson's ratios of both sample and tip.

Due to the method's dependence on the geometry of the indenting tip, any divergence from the ideal shape must be recorded and used to correct the projected areas. As the projected areas are extracted from the indentation depth, any errors in this will also affect the measurement. Besides surface roughness,

two commonly occurring behaviours are *sink-in* and *pile-up*. In sink-in the real area of contact is reduced because the surface bends in instead of forming an edge at the indenter edge. In pile-up the actual area of contact is increased as the indented material flows and buckles up around the indenter. These behaviours are not directly detectable from the load-displacement curves and must be verified by microscopy.

Measuring the hardness of a thin film poses extra difficulties in that care must be taken to measure only the film and not the substrate. In practice this means reducing the load and indentation depth so as not to affect the substrate; a typical test is to do a range of maximum loads from low to high which should give two plateaus representing the film and substrate with a transition region in between. The sharpness of the tip and the stability of the instrument determine how thin samples may be analyzed. A common rule of thumb is to have a maximum penetration depth less than 10 % of the film thickness, and for ease of measurement, a film thickness of 1 μm is often desirable.

Summaries of Included Papers

6

6.1 Paper I

TiSiCN hard coatings, with varying Si and C contents, deposited by cathodic arc evaporation were investigated. The films were of a B1 NaCl phase with Si contents ranging from 0-7 at. %. The microstructures were dense columnar, with a column diameter of approximately 100 nm. The high-Si-content films also exhibited a nanostructure, with a featherlike contrast in the TEM, and this nanostructure was promoted by the addition of C to the films. The hardnesses of the films were 32-40 GPa, and were influenced by both the Si and C contents. Age hardening was observed upon annealing with a peak hardness of 44 GPa. The over-ageing threshold temperature was found to decrease with increasing C and Si content, due to loss of Si from the film and interdiffusion Co, W and Cr from the substrate.

6.2 Paper II

High Al-content $Zr_{0.44}Al_{0.56}N_{1.20}$ was synthesized by cathodic arc evaporation. The as-deposited film exhibited a segregated nanostructure consisting of defect-rich NaCl and wurtzite phases, with grain sizes around 3-5 nm. Annealing to 1000 °C caused recovery of the Zr-rich cubic ZrAlN phase, and release of the excess N. This resulted in age hardening of the film from 20 to 28 GPa. Further annealing to 1200 °C caused recrystallization of w-AlN and a resulting over-ageing of the film.

6.3 Paper III

$Ti_{0.33}Al_{0.67}N$ solid solution thin films deposited by cathodic arc evaporation were analysed by atom probe tomography. Both an as-deposited film and a

film annealed to 900 °C were studied. The annealed film showed a clear decomposition on the metal sublattice, that was determined to stem from spinodal decomposition. The as-deposited film also exhibited minor, but significant, fluctuations on the metal sublattice. The N composition was determined to co-vary with the Al content in the annealed film; the stoichiometric condition of AlN and the wider stability region of TiN present a way for the system to locally accommodate coherency strains between the decomposed domains.

References

[1] Modern Metal Cutting – A Paractical Handbook (1996). Sandviken Coromant, Sandviken.

[2] M Paulsson and C Richt (2007). The Development of Coated Grades of Carbide Tools. *American Machinist, 12*.

[3] D A Stephenson and J S Agapiou (2006). *Metal Cutting Theory and Practice*. CRC Press.

[4] J E Sundgren (1985). Structure and Properties of TiN Coatings. *Thin Solid Films, 128*(1-2), 21–44.

[5] L Hultman (2000). Thermal Stability of Nitride Thin Films. *Vacuum, 57*(1), 1–30.

[6] Louis E Toth (1971). *Transition Metal Carbides and Nitrides*. Academic Press, New York.

[7] Lennart Karlsson *Arc Evaporated Titanium Carbonitride Coatings*. PhD thesis, Linköping University.

[8] Anders Hörling (2005). *Thermal Stability and Age Hardening of TiN-Based Thin Films*. PhD thesis, Linköping University.

[9] Axel Flink (2008). *Growth and Characterization of Ti-Si-N Thin Films*. PhD thesis, Linköping University.

[10] G Beenshmarchwicka, L Krolstepniewska and W Posadowski (1981). Structure of Thin-Films Prepared by the Cosputtering of Titanium and Aluminum or Titanium and Silicon. *Thin Solid Films, 82*(4), 313–320.

[11] W D Münz (1986). Titanium Aluminum Nitride Films: A New Alternative to TiN Coatings. *Journal of Vacuum Science & Technology A: Vacuum, 4*(6), 2717–2725.

[12] U Wahlström, L Hultman, J E Sundgren, F Adibi and I Petrov et al. (1993). Crystal-Growth and Microstructure of Polycrystalline $Ti_{1-X}Al_xN$ Alloy-Films Deposited by Ultra-High-Vacuum Dual-Target Magnetron Sputtering. *Thin Solid Films, 235*(1-2), 62–70.

[13] A Hörling, L Hultman, M Odén, J Sjölén and L Karlsson (2005). Mechanical Properties and Machining Performance of $Ti_{1-x}Al_xN$-Coated Cutting Tools. *Surface & Coatings Technology, 191*(2-3), 384–392.

[14] Hans Söderberg (2006). *Growth and Characterization of TiN/*SiN_x *Multilayer Thin Films*. PhD thesis, Luleå University of Technology.

[15] H Ljungcrantz, M Odén, L Hultman, J E Greene and J E Sundgren (1996). Nanoindentation studies of single-crystal (001)-, (011)-, and (111)-oriented TiN layers on MgO. *Journal of Applied Physics, 80*(12), 6725–6733.

[16] B Alling, A V Ruban, A Karimi, O E Peil and S I Simak et al. (2007). Mixing and decomposition thermodynamics of c-$Ti_{1-x}Al_xN$ from first-principles calculations. *Physical Review B, 75*(4), 45123.

[17] PDF-card No. 30-0753 (1998). JCPDS - International Centre for Diffraction Data.

[18] PDF-card No. 38-1420 (1998). JCPDS - International Centre for Diffraction Data.

[19] PDF-card No. 46-1200 (1998). JCPDS - International Centre for Diffraction Data.

[20] M Wong, G Hsiao and S Yang (2000). Preparation and characterization of AlN/ZrN and AlN/TiN nanolaminate coatings. *Surface and Coatings Technology, 133-134*, 160-165.

[21] L Shizhi, S Yulong and P Hongrui (1992). Ti-Si-N films prepared by plasma-enhanced chemical vapor deposition. *Plasma Chemistry and Plasma Processing, 12*, 287-297.

[22] S Vepřek, S Reiprich and L Shizhi (1995). Superhard nanocrystalline composite materials: The TiN/SiN system. *Applied Physics Letters, 66*, 2640.

[23] DV Shtansky, EA Levashov, AN Sheveiko and JJ Moore (1999). Synthesis and characterization of Ti-Si-C-N films. *Metall Mater Trans A, 30*(9), 2439–2447.

[24] D Kuo and K Huang (2001). A new class of Ti-Si-C-N coatings obtained by chemical vapor deposition. *Thin Solid Films, 394*, 72–80.

[25] D A Porter, K E Easterling and M Y Sherif (2009). *Phase Transformations in Metals and Alloys*. CRC Press, London.

[26] J W Gibbs (1961). *The Scientific Papers of J Willard Gibbs*. Dover Publications, New York.

[27] John Cahn (1961). On Spinodal Decomposition. *Acta Metallurgica, 9*(9), 795–801.

[28] John W Cahn (1966). The Later Stages of Spinodal Decomposition and the Beginnings of Particle Coarsening. *Acta Metallurgica, 14*, 1685–1692.

[29] A Anders (2002). Energetic Deposition Using Filtered Cathodic Arc Plasmas. *Vacuum, 67*, 673-686.

[30] P. B. Barna and M. Adamik (1998). Fundamental structure forming phenomena of polycrystalline films and the structure zone models. *Thin Solid Films, 317*(1-2), 27–33.

[31] I Petrov, P B Barna, L Hultman and J E Greene (2003). Microstructural Evolution during Film Growth. *J Vac Sci Technol A, 21*(5), S117–S128.

[32] T Kelly and M Miller (2007). Invited Review Article: Atom Probe Tomography. *Review of Scientific Instruments, 78*, 31101.

[33] M K Miller and R G Forbes (2009). Atom Probe Tomography. *Materials Characterization, 60*(6), 461–469.

[34] F Vurpillot, F De Geuser, G Da Costa and D Blavette (2004). Application of Fourier Transform and Autocorrelation to Cluster Identification in the Three-Dimensional Atom Probe. *Journal of Microscopy, 216*(3), 234–240.

[35] Baptiste Gault, Frederic De Geuser, Leigh T Stephenson, Michael P Moody and Barrington C Muddle et al. (2008). Estimation of the Reconstruction Parameters for Atom Probe Tomography. *Microscopy and Microanalysis, 14*(04), 1–10.

[36] Baptiste Gault, Michael P Moody, Frederic De Geuser, Daniel Haley and Leigh T Stephenson et al. (2009). Origin of the Spatial Resolution in Atom Probe Microscopy. *Applied Physics Letters, 95*(3), 034103.

[37] Thomas F Kelly, Tye T Gribb, Jesse D Olson, Richard L Martens and Jeffrey D Shepard et al. (2004). First Data from a Commercial Local Electrode Atom Probe (LEAP). *Microscopy and Microanalysis, 10*(03), 1–11.

[38] RG Forbes (1995). Field Evaporation Theory: A Review of Basic Ideas. *Applied Surface Science, 87*, 1–11.

[39] David Kingham (1982). The Post-Ionization of Field Evaporated Ions: A Theoretical Explanation of Multiple Charge States. *Surf Sci, 116*(2), 273–301.

[40] P Bas, A Bostel, B Deconihout and D Blavette (1995). A General Protocol for the Reconstruction of 3d Atom Probe Data. *Applied Surface Science, 87*, 298–304.

[41] D Larson, D Foord, A Petford-Long and T Anthony et al. (1998). Focused Ion-Beam Milling for Field-Ion Specimen Preparation:-Preliminary Investigations. *Ultramicroscopy, 75*, 147-159.

[42] Michael K Miller, Kaye F Russell, Keith Thompson, Roger Alvis and David J Larson (2007). Review of Atom Probe Fib-Based Specimen Preparation Methods. *Microscopy and Microanalysis, 13*(06), 1–9.

[43] W C Oliver and G M Pharr (1992). An Improved Technique for Determining Hardness and Elastic-Modulus Using Load and Displacement Sensing Indentation Experiments. *Journal of Materials Research, 7*(6), 1564–1583.